2018-01-0202 Published 03 Apr 2018

Large-Eddy Simulation and Analysis of Turbulent Flows in a Motored Spark-Ignition Engine

Devyani Patil, Yue Wang, Long Liang, Karthik Puduppakkam, Ahmed Hussein, Chitralkumar Naik, and Ellen Meeks ANSYS Inc

Citation: Patil, D., Wang, Y., Liang, L., Puduppakkam, K. et al., "Large-Eddy Simulation and Analysis of Turbulent Flows in a Motored Spark-Ignition Engine," SAE Technical Paper 2018-01-0202, 2018, doi:10.4271/2018-01-0202.

Abstract

Advanced research in Spark-ignition (SI) engines has been focused on dilute-combustion concepts. For example, exhaust-gas recirculation is used to lower both fuel consumption and pollutant emissions while maintaining or enhancing engine performance, durability and reliability. These advancements achieve higher engine efficiency but may deteriorate combustion stability. One symptom of instability is a large cycle-to-cycle variation (CCV) in the in-cylinder flow and combustion metrics. Large-eddy simulation (LES) is a computational fluid dynamics (CFD) method that may be used to quantify CCV through numerical prediction of the turbulent flow and combustion processes in the engine over many engine cycles.

In this study, we focus on evaluating the capability of LES to predict the in-cylinder flows and gas exchange processes in a motored SI engine installed with a transparent combustion chamber (TCC), comparing with recently published data. Numerical simulations are performed using the commercial CFD software, ANSYS Forte, employing a classical Smagorinsky sub-grid-scale (SGS) model for the LES approach. Two important aspects of the model, namely the coefficient of sub-grid viscosity used in the Smagorinsky model, and the numerical scheme for discretizing the convection term in the momentum transport equation, are evaluated.

Simulations are performed for 20 consecutive engine cycles after the simulation setup is validated by the predicted in-cylinder pressure, trapped mass, and temperature data. LES-predicted phase-averaged-mean and root-mean-square (RMS) velocity fields are compared with high-speed particle image velocimetry (PIV) data. The comparison and analysis are performed at two crank angles, representing intake and compression strokes, and on two different planes for measurement in the engine combustion chamber. A proper orthogonal decomposition (POD) technique is applied to quantify CCV in both the LES results and the PIV data, to provide a quantitative assessment of the predictions from LES. The flow field statistics predicted by the LES-Smagorinsky model match well with experimental results. Based on these simulation results, optimal practices for the use of Smagorinsky model with respect to the numerical schemes are summarized.

Introduction

Due to extensive use of Spark-ignition (SI) engines in transportation, it is important to improve engine efficiency and to drastically reduce fuel consumption as well as emissions. To achieve this aim, research is being conducted on the "dilute combustion" techniques in SI engines [1]. The state of dilute combustion can be achieved by either lean burning of fuel or by using exhaust gas recirculation. Even though results obtained with dilute combustion are encouraging, there are some drawbacks too. Dilute combustion enhances variations in key combustion characteristics, such as ignition delay and combustion duration, in different engine cycles. Variations in flow and combustion events and outcomes between different engine cycles but under the same operating conditions is known as cycle-to-cycle variation (CCV) or cyclic variability. To name a few undesirable outcomes of CCV, certain cycles burn faster, which results in higher peak pressure as compared to average and increases the risk of knocking; on the other extreme, certain cycles have slower combustion causing partial burning or even misfire. The existence of CCV in combustion has a negative impact on the overall engine performance characteristics, leading to increases in pollutant emissions, engine noise and vibration, and a reduction in fuel economy.

In-depth analysis of the physical and chemical processes in SI engines concludes that one of the main causes of the CCV in combustion characteristics is cyclic variation in the in-cylinder flow field during gas exchange processes [2]. To address the challenges of CCV and to improve the dilute combustion techniques, it is critical for engineers to quantify the extent and degree of CCV and to predict how it responds to changes in engine design parameters.

Computational fluid dynamics (CFD) has been increasingly used as a predictive tool to study the turbulent flow and combustion processes in engines. However, predicting CCV numerically remains a challenging task, due to the difficulty in resolving the unsteady and turbulent flows for many engine cycles within a reasonable turn-around time. The Large-eddy simulation (LES) approach is a useful modeling technique in simulating the instantaneous flows of each engine cycle and

predicting the temporally and spatially varying flow structures. Analyzing simulation results over many engine cycles allows CCV to be predicted and quantified.

To briefly review the use of LES in internal combustion (IC) engine research, Haworth [3] introduced LES in his simulation of engine flows using an affordable CFD mesh size. He showed that LES offered more realistic representation of the complex in-cylinder flows as compared to the Reynolds-Averaged-Navier-Stokes (RANS) approach, which represents the ensemble-averaged flow field. Rutland [4] reviewed different types of LES models and discussed their advantages and disadvantages when applied to engine simulations. Yang *et al.* [5] performed a comparative study between LES and RANS for a motored engine flow simulation. They concluded that although both LES and RANS captured the overall trend in mean flows qualitatively, LES was more accurate in capturing instantaneous flow field than RANS. Also, they found that the in-cylinder flow patterns could be captured by the simulations when partial intake and exhaust port geometry with appropriate inflow and outflow conditions were used. In another study, Kuo *et al.* [6] presented a rigorous procedure to quantify and analyze the flow field results of a LES simulation. They also concluded that the simulation results from 10 consecutive engine cycles were sufficient in representing the full ensemble of cycles and for quantifying the predicted CCV and other statistical aspects of the flow field. Ameen *et al.* [7] presented a parallel methodology to conduct LES simulations in multiple non-consecutive engine cycles with statistically-varied initial conditions. They presented that by perturbing initial velocity flow field, overall mean and RMS flow filed of simulation can be captured reasonably well within less computational time. A number of studies adopted this type of Parallel Perturbation Methodology (PPM) [8, 9, 10, 11] for LES simulation. Tsang *et al.* [12] evaluated and validated various LES models using several shear-intensive flow problems that are important to the engines, such as gas jets, sprays and diffusion flames. They also discussed the effects of CFD mesh size and different numerical schemes for momentum convection. Zhao *et al.* [13] studied CCV in a fired SI engine using LES and a G-equation combustion model. They demonstrated that the variations in flow velocity around the spark plug region during ignition are the main causes for the variations in the burn rates after ignition.

To gain confidence in LES for IC engine simulations, it is important to validate the simulation results against detailed measurement data of the turbulent flow field. In several studies that focused on simulations [5], [6], [7], [8], [9], [10], [11], the same experimental flow field data from a motored SI optical engine was used. This optical engine, which will be reviewed in the next section, has been continuously developed at the University of Michigan, and the flow field data was measured by the high-speed particle image velocimetry (PIV) technique. Schiffmann *et al.* [14] described efforts to benchmark the engine along with applying the experimental data for the verification and validation of LES simulations. Ruess [15] presented two-dimensional PIV data and measured cyclic variability by capturing velocity distributions for directed flow (using shrouded valve), and undirected flow (using a standard valve). Van Dam *et al.* [16] performed LES simulation at motored engine condition and the results were compared with the PIV data. They also presented circular standard deviation as a method to identify critical flow structures.

Proper orthogonal decomposition (POD) is an analytical tool to extract useful statistical information from the results of multiple engine cycles and compare the extracted data from both experiments and simulations. Chen *et al.* [17] presented the mathematical concept and properties of POD, and demonstrated that the first "mode" from the POD analysis contained flow structures similar (but not identical) to those of the ensemble-average, with almost equal mass-specific kinetic energy. Liu and Haworth [18] presented POD analysis of a statistically non-stationary flow simulation in a well-defined and simple time-dependent domain. Chen *et al.* [19] demonstrated that POD could explicitly separate the ensemble-averaged kinetic energy from the turbulent fluctuation of kinetic energy on a cycle-to-cycle basis. Buhl *et al.* [20] applied POD along with conditional averaging to quantify CCV from the turbulent flow data. They identified fluctuations in large-scale flow structures in IC engines and emphasized the difference between cyclic fluctuations of coherent motions and turbulent fluctuations in general.

In this work, we focus on simulating multiple cycles of turbulent flows in a motored SI optical engine, and systematically evaluating the LES predictions against the measured data. First, the experimental engine setup and operating conditions are described, followed by a discussion of turbulence modelling approach using LES. Next, the statistical analysis method and POD technique are discussed. Information of simulation setup, which includes geometry, meshing, initial and boundary conditions, follows. Finally, simulation results and comparative analysis between LES and PIV data are presented, followed by the summary and conclusions.

Experimental Setup

The present study uses experimental data obtained from an optical engine, created to generate detailed and quantitative data for the in- cylinder and gas exchange flows in the engine and support the development and validation of turbulence modeling approaches. The engine, termed as "TCC-III" [21], [22], is installed with a transparent combustion chamber to allow high optical accessibility for flow field measurements.

The test setup consists of a single cylinder engine with pancake-shaped piston in a transparent combustion chamber. A spark plug is placed at the center of the cylinder head. The combustion chamber is installed with one intake and one exhaust valve, which are connected via runners to intake and exhaust plena, respectively. Figure 1 shows a sketch of all the components in the test arrangement.

The engine has been tested for a range of operating conditions. For this study, we use results obtained with 1300 rpm speed and average intake plenum pressure of 40 kPa. The engine geometry parameters and valve timings are summarized in Table 1. More TCC engine specifications are discussed in detail by Sick *et al.* [21] and are also available on the University of Michigan website [22].

FIGURE 1 Experimental Setup of TCC III engine [22]

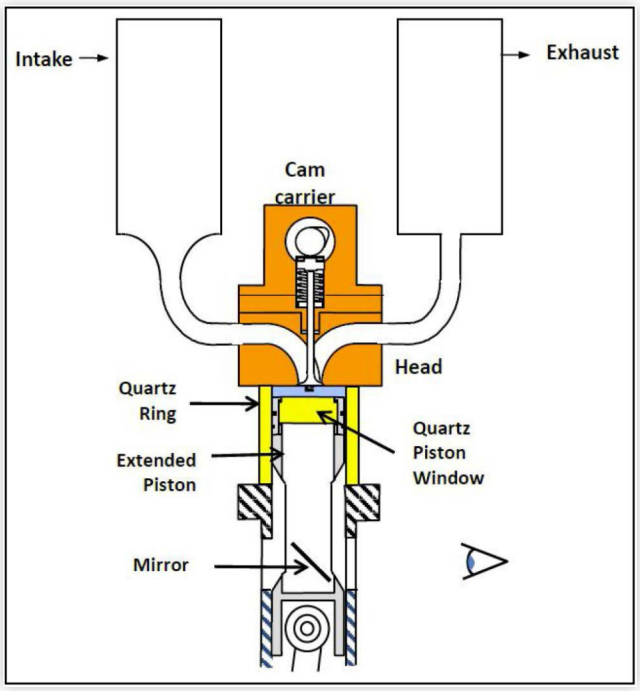

TABLE 1 TCC III engine geometry specification and valve timings [22]

Bore	9.20 cm
Stroke	8.60 cm
Connecting rod length	23.10 cm
Geometric Compression Ratio	10.0
Effective Compression Ratio	8.6
Combustion chamber	63.15 cm^3
Clearance Volume at TDC	0.95 cm^3
Exhaust Valve Closing	12.8 degrees ATDC
Intake Valve Closing	240.8 degrees ATDC
Exhaust Valve Opening	484.8 degrees ATDC
Intake Valve Opening	712.8 degrees ATDC

The PIV method has been employed to measure instantaneous and phase-averaged velocity components of the in-cylinder flow on several two-dimensional planes. Figure 2 shows locations of the PIV measurement planes with respect to the engine cylinder geometry. PIV velocity data for all planes are available for consecutive cycles at every 5 crank angle degrees [22]. The approach of conducting PIV measurements, post processing and its properties are explained broadly by Abraham *et al.* [23]. All the experimental data used in this paper is downloaded from [22].

Simulation Approach

This study uses the commercial CFD software ANSYS Forte [24] to simulate the motored engine flows in the TCC-III engine. Forte solves multi-dimensional, finite-volume-based compressible flow equations for reacting flows and sprays in the IC engine. The spatial accuracy in solving the governing equations is 2nd order, and the temporal accuracy is 1st order. The solver automatically generates strictly Cartesian mesh to discretize the simulation domain and adaptively refines the mesh based on evolving flow solutions. An immersed boundary method is employed to enforce boundary conditions on the physical surface geometry not aligned with the Cartesian mesh. In previous work [12], the software's capability of simulating turbulent flows was validated by several fundamental flow problems, such as backwards-step flow, gas jets, evaporating sprays, reacting sprays and turbulent diffusion flames.

FIGURE 2 PIV measurement planes used to collect flow velocity data in the TCC-III motored engine flow experiment [10]

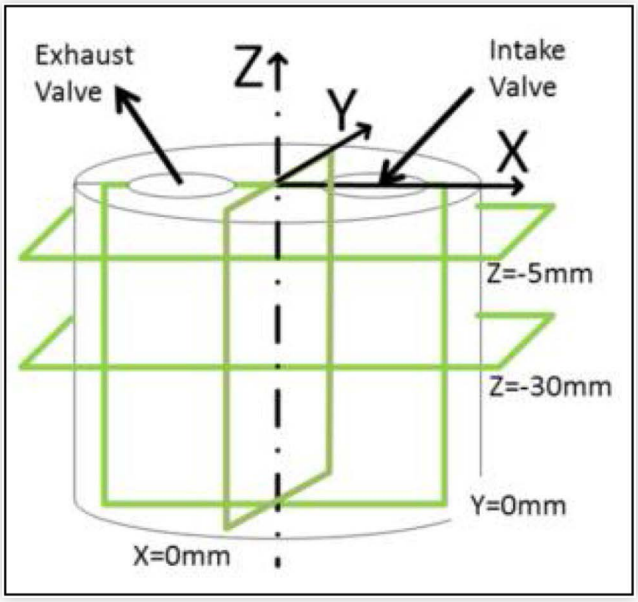

LES Sub-Grid Scale (SGS) Model

An LES model resolves large-scale flow structures (or "eddies") by explicitly solving the governing equations of fluid mechanics on the CFD mesh, and predicting the flow structures smaller than the local mesh size by models. The mesh effectively works as an implicit "filter", and any flow field quantities discretized and defined on the mesh are regarded as filtered quantities. Mathematically, an "exact" flow field quantity (*e.g.* velocity) can be divided into two parts, a filtered component representing the resolved part and a residual component representing the "sub-grid" part. The governing equations under the LES context are obtained by applying the filter to the Navier-Stokes equations. The filtered momentum equation is written as:

$$\frac{\partial \bar{\rho}\tilde{\mathbf{u}}}{\partial t} + \nabla\cdot\left(\bar{\rho}\tilde{\mathbf{u}}\tilde{\mathbf{u}}\right) = -\nabla\bar{p} + \nabla\cdot\bar{\rho}\nu\left(\nabla\tilde{\mathbf{u}} + \left(\nabla\tilde{\mathbf{u}}\right)^T - \frac{2}{3}\nabla\cdot\tilde{\mathbf{u}}\mathbf{I}\right) - \nabla\cdot\bar{\rho}\boldsymbol{\tau} \quad (1)$$

in which $\bar{\rho}$ is the filtered density, $\tilde{\mathbf{u}}$ is the Favre-averaged filtered velocity ($\tilde{\mathbf{u}} = \overline{\rho\mathbf{u}} / \bar{\rho}$), $\bar{p}$ is the filtered pressure, and ν is the kinematic molecular viscosity. The filtered equations are arranged to achieve resemblance to an unfiltered Navier-Stokes equation, but with an additional term of residual stress tensor representing sub-grid scale (SGS) effects. The SGS stress tensor $\boldsymbol{\tau}$ is defined as:

$$\tau_{ij} \equiv \left(\widetilde{u_i u_j} - \tilde{u}_i \tilde{u}_j \right) \tag{2}$$

Modelling of the SGS stress tensor is necessary to close the momentum equation and thus to solve for the filtered velocity field. The present study uses the Smagorinsky model for this purpose.

Smagorinsky Model

The Smagorinsky model uses the mathematical version of Bossinesq hypothesis that turbulent fluctuations are dissipative in nature and can be modeled by diffusion. The SGS stress is assumed to be directly proportional to the filtered rate of strain:

$$\tau_{ij} = -2\nu_{sgs}\left(\tilde{S}_{ij} - \frac{1}{3}\tilde{S}_{kk}\delta_{ij} \right) + \frac{1}{3}\tau_{kk}\delta_{ij} \tag{3}$$

where $\tilde{S}_{ij}$ is the filtered strain rate tensor, $\tilde{S}_{ij} = \frac{1}{2}\left(\partial\tilde{u}_i / \partial x_j + \partial\tilde{u}_j / \partial x_i \right)$. $\tau_{kk} = 2k_{sgs}$, in which k_{sgs} is the sub-grid kinetic energy. The sub-grid viscosity, ν_{sgs}, acts as a modeled viscosity to account for the effects of momentum transfer due to turbulent motion:

$$\nu_{sgs} = \left(C_s \Delta \right)^2 \left| \tilde{S} \right| \tag{4}$$

in which Δ is the filter width as well as the local CFD grid size, $\left| \tilde{S} \right| = \left(2\tilde{S}_{ij}\tilde{S}_{ij} \right)^{1/2}$ is the magnitude of the strain rate, and C_s is a model constant with a default value of 0.17.

A familiar issue with the Smagorinsky model is that it is purely dissipative in modeling the effects of sub-grid turbulent motions. As a result, a fine mesh size is often required to resolve the small-scale flow structures adequately. However, because of its numerical stability in complex flows and geometries, the Smagorinsky model is still one of the most commonly used LES SGS models in solving engineering flow problems. Therefore, it is chosen as the baseline approach in the present work. Here, we have focused on presenting the SGS model used in the momentum equation. The Smagorinsky model employs viscosity-based SGS models in the mass and energy transport equations, with standard turbulent Schmidt and Prandtl numbers associating the SGS diffusivity and heat conductivity with the viscosity ν_{sgs}.

Another LES model called "implicit LES" is also adopted to compare with the standard Smagorinsky model. By setting the model constant C_s in Eq. (4) as zero, this model effectively removes the SGS stress term from the filtered momentum equation. The effects of sub-grid motions on large-scale momentum transfer are accounted for by the numerical effects of discretization, rather than physics-based assumptions. Using this approach removes the concern about the Smagorinsky model being overly dissipative in solving for the large-scale motions.

Numerical Schemes for Momentum Convection

In turbulent flows, convection is a dominating mechanism of momentum transport. Accurate calculation of the convection term in Eq. (1) is important since it affects the resolution of large-scale flow motions and the turbulent transport processes. In the finite-volume method, to calculate convection across neighboring cells, variables at the cell faces shared by neighboring cells must be properly modeled. Taking a 1-D situation as an example, the flow quantity ϕ (*i.e.*, velocity component) at a cell face a shared by two adjacent control volumes centered at x_i and x_{i+1} is calculated by a 1st-order Taylor series expansion of the cell-centered solutions:

$$\phi_\alpha = \begin{cases} \phi_i + \left.\dfrac{\partial\phi}{\partial x}\right|_i \left(x_\alpha - x_i \right)\left(1 - \dfrac{\delta V_\alpha}{V_i} \right), if\ \delta V_\alpha > 0 \\ \phi_{i+1} - \left.\dfrac{\partial\phi}{\partial x}\right|_{i+1} \left(x_{i+1} - x_\alpha \right)\left(1 + \dfrac{\delta V_\alpha}{V_{i+1}} \right), if\ \delta V_\alpha < 0 \end{cases} \tag{5}$$

where δV_α is the flux volume, taken as positive if cell i is upwind. In the QSOU scheme, the gradient of solutions is calculated as:

$$\left.\frac{\partial\phi}{\partial x}\right|_i = \begin{cases} sign\left(\Delta\phi_i \right) min\left(\dfrac{\left|\Delta\phi_i\right|}{\Delta x_i}, \dfrac{\left|\Delta\phi_{i-1}\right|}{\Delta x_{i-1}} \right) if\ \Delta\phi_i\, \Delta\phi_{i-1} > 0 \\ 0\ if\ \Delta\phi_i\, \Delta\phi_{i-1} < 0 \end{cases} \tag{6}$$

in which $\Delta\phi_i = \phi_{i+1} - \phi_i$. The scheme conditionally uses the interpolation to calculate ϕ_α based on the monotonicity of local variables. When the variation of ϕ is not monotone, it is reduced to an upwind scheme [25].

The central differencing scheme always computes the gradient by the neighboring quantities without upwind preference, and is strictly 2nd order accurate:

$$\left.\frac{\partial\phi}{\partial x}\right|_i = \frac{\phi_{i+1} - \phi_{i-1}}{x_{i+1} - x_{i-1}} \tag{7}$$

The central differencing scheme has higher order of accuracy than QSOU and is thought to be beneficial in predicting turbulent transport in certain shear-intensive flow problems [26], [12], but the QSOU scheme is more stable than CD, due to its monotonic nature.

Wall Boundary Conditions

Law-of-the-wall relations are used to model the momentum and heat transport in turbulent boundary layers and predict the shear stress and heat transfer at physical wall boundary. While the Law-of-the-wall relations represent ensemble-average, they are useful in the current LES simulation where engineering mesh resolution is employed. The near-wall mesh size effectively filter away local flow structures of sub-grid size, which also fluctuate in time with related time scales. In this sense, the filtering in near-wall mesh is equivalent to

an ensemble average, and this justifies use of Law-of-the-wall as wall boundary conditions in LES. Details of the relations are summarized in [24].

Analysis of Turbulent Flow Field

Relevance Index

A Relevance index is used to quantify the degree of similarity between flow structures in two flow fields. It is calculated by projecting one flow field onto the other and then normalizing, as follows:

$$R_p = \frac{(\mathbf{u},\mathbf{v})}{\|\mathbf{u}\|\|\mathbf{v}\|} \tag{8}$$

in which **u** and **v** are two flow velocity fields that are supposed to be relevant to each other, *e.g.*, one being the velocity field from simulation and the other from experiment. The (•) operator in the numerator denotes inner product, and ||•|| in the denominator indicates L^2 norms. The value of R_p varies between +1 to −1. "+1" indicates that two flow field have perfectly aligned flow structures everywhere, whereas "-1" indicates that the flow structures are in exactly opposite directions. If the flow structures are orthogonal, the value of relevance index is 0. Relevance index is not affected by the kinetic energy contained in the flow. In other words, two velocity fields with R_p equal to 1 can have different magnitudes of velocity.

Proper Orthogonal Decomposition (POD)

To analyze the turbulent flow field from many engine cycles and to extract meaningful statistical information, the POD method is used. The main procedures of POD are outlined as follows, while more detailed information regarding its theoretical background is reported elsewhere [17], [18], [19].

At a specific crank angle degree during an engine cycle, we denote the two-dimensional velocity field on one of the measurement planes shown in Figure 2 as a "snapshot" of the flow field. The velocity field taken on the same plane and at the same crank angle from different engine cycles constitute a data set of snapshots, which serve as the basis of POD analysis. We denote V as one component of the velocity vector, and $V(k)$ as the velocity field of the kth snapshot (k = 1 to K, where K is the number of snapshots or engine cycles studied). POD analysis decomposes $V(k)$ into a linear combination of weighted spatial basic functions called "modes" (fm), each of which has corresponding time-dependent coefficient, C_m^k:

$$V(k) = \sum_{m=1}^{M} C_m^k f^m \tag{9}$$

For the current IC engine application, the "method of snapshots" introduced by Sirovich [27] is used. The method of snapshots is more efficient in cases where the number of instances in time at which velocity is measured are less than the number of spatial locations where measurement takes place. In this method, the number of snapshots (or engine cycles) (K) is equal to the number of modes (M). The modes are not specified *a priori*; instead, they are computed using the snapshots' data such that the following function is minimized:

$$\sum_{k=1}^{K} \| \left[V(k) - \sum_{m=1}^{M} C_m^k f^m \right] \|^2 \rightarrow min$$

$$\text{Subject to the condition that } \left(f^i, f^j\right) = \delta_{ij} = \begin{cases} 1 \; if \; i = j \\ 0 \; if \; i \neq j \end{cases} \tag{10}$$

Each mode represents a basic flow structure extracted from the snapshots. The ensemble of mutually orthogonal and normalized modes ($f^1 f^2 \ldots \ldots fM$) is represented by a two-dimensional matrix of $M \times J$, where J is the number of locations on the measurement plane used to collect velocity data. The coefficients C_m^k forms a matrix of $K \times M$ size, which are calculated by projecting the velocity vector $V(k)$ onto mode fm. The square of the coefficient $\left(C_k^m\right)^2$ determines the contribution in mass-specific kinetic energy from the m^{th} mode into k^{th} snapshot. Values of coefficients can be positive or negative. As a result, the "energy" of a single snapshot can be calculated by:

$$E_k = \frac{1}{2} \sum_{m=1}^{M} \left(C_m^k\right)^2 \tag{11}$$

The energy of a single mode is given by:

$$E_m = \frac{1}{2} \sum_{k=1}^{K} \left(C_m^k\right)^2 \tag{12}$$

The energy fraction of each mode is:

$$e_m = E_m / \sum_{m=1}^{M} E_m \tag{13}$$

POD modes are optimal such that the 1st mode contains the largest fraction of energy and most of the flow's kinetic energy is represented by the first few modes.

The modes obtained from POD analysis of any two separate data sets at a specific crank angle can be compared by means of energy spectra (energy or cumulative energy fraction versus mode number) and relevance index. Energy spectra indicates how much energy is contained in each mode in the two data sets, respectively, whereas the relevance index quantifies the degree of structural similarity between the two. Like any statistical method, if the two data sets are to be compared unambiguously by POD, they must have the same number of snapshots and the flow field data must be collected from identical locations.

Another objective of using POD analysis for the CCV study is to quantify each cycle's contribution to the ensemble-averaged and Root-Mean-Squared (RMS) flows. Chen et al. [19] and Buhl et al. [20] discussed the separation of contributions from each cycle to the ensemble-averaged kinetic energy and RMS kinetic energy due to turbulence fluctuation,

with respect to the total kinetic energy. The kinetic energy contained in the ensemble-averaged flow field is given as:

$$\mathrm{KE}_{\mathrm{avg}} = \frac{1}{2K}\sum_{k=1}^{K}\left(C_1^k\right)^2 \tag{14}$$

Thus, the kinetic energy of the 1st mode from all the data snapshots can be used to estimate the contribution of each cycle k to the ensemble-averaged kinetic energy. Turbulence fluctuation energy is estimated as:

$$\mathrm{KE}_{\mathrm{turb}} = \sum_{m=2}^{M}\left[\frac{1}{2K}\sum_{k=1}^{K}\left(C_m^k\right)^2\right] \tag{15}$$

Thus, coefficients of modes 2 → M can be used to calculate the contribution to the turbulent kinetic energy from each cycle.

In this study, to compare the LES flow field characteristics against the PIV measurements, snapshots of velocity flow field at two measurement planes, Y = 0 mm and X = 0 mm (Figure 2), are taken for each engine cycle, and these snapshots are used as input for the POD analysis.

Computational Setup

Instead of using the full experimental geometry containing the intake and exhaust plenums (Figure 3), our computational domain includes the full combustion chamber enclosed by the cylinder head, spark plug, liner, piston and valves, as well as part of the intake and exhaust ports (Figure 4). The intake and exhaust plenums are omitted, and the pressure inflow and outflow values at those locations are applied as boundary conditions on the cut-planes that separate the modeled partial ports from the omitted parts. Cycle-independent pressure and temperature boundary conditions at the inlet and outlet

FIGURE 3 Full CFD computational domain including intake and exhaust plenums.

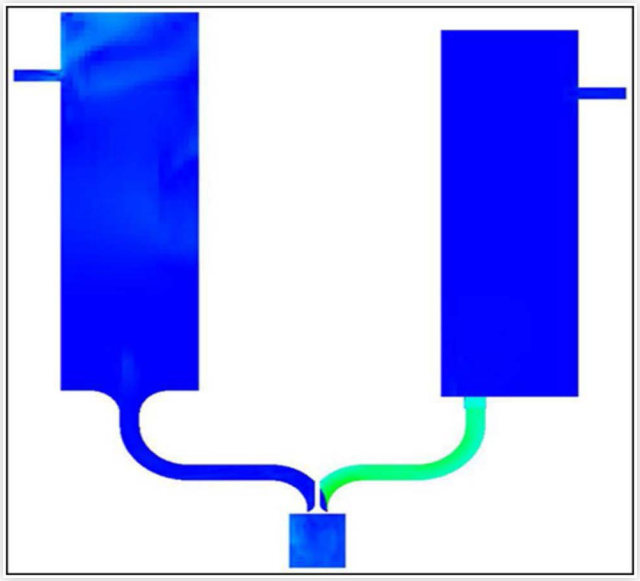

FIGURE 4 Modified computational domain with parts of the intake and exhaust ports omitted to save computational cost. Pressure and temperature boundary conditions are applied on the inflow and outflow boundary in the ports.

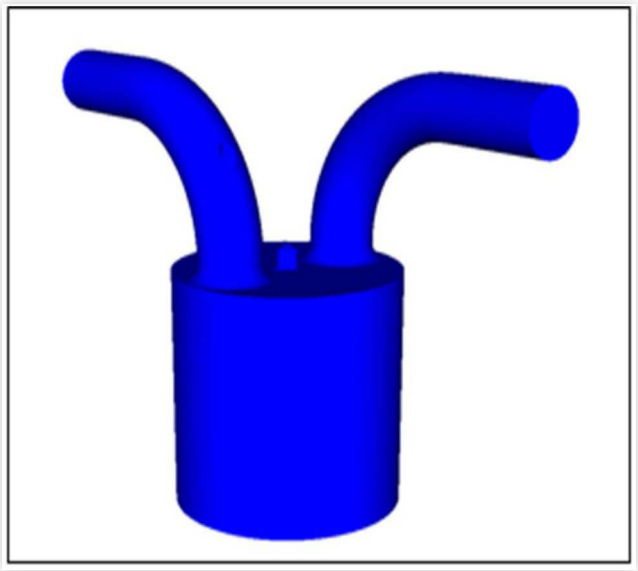

are available from the engine's system-level simulation results [22]. A similar partial simulation domain has been used in the works of Yang *et al.* [5], Kuo *et al.* [6] and Ameen *et al.* [7]. These studies showed that even though CFD simulation using partial geometry introduce simplification to the intake and exhaust flows, obtained results are qualitatively comparable to the experimental data, with all the major flow structures during an engine cycle resolved correctly.

ANSYS Forte automatically generates and updates the volume mesh with perfectly orthogonal Cartesian cells on-the-fly, during the simulation. Solution-adaptive meshing (SAM) [28] is used throughout the simulation. SAM refines the mesh in response to the local variation of a solution field or its gradient to resolve the meaningful flow structures as they evolve with time. The inputs for SAM include choice of solution variable to which the meshing adapts, refinement criteria, and the desired refinement level. Cells meeting the refinement criteria at a given time step will be refined to the desired mesh size specified as input. Previously refined cells that no longer meets the solution criteria will be coarsened up to the default mesh size, unless influenced by another mesh control. The main advantage of implementing SAM is that mesh refinement takes place only in the solution intensive regions where a finer mesh is required for better accuracy. Application of SAM helps to significantly reduce the total cell count and computational time while maintaining solution accuracy of turbulent flows [12].

Since this study concerns motored-engine flows, SAM has been imposed only for the gradient of flow velocity. A statistical refinement criterion is used such that cells with velocity gradient values greater than a low threshold value but less than a high threshold will undergo refinement. The threshold values are given by:

$$x_{low\_threshold} = x_{mean} + c_{threshold}\cdot\sigma x_{high\_threshold} = +\infty \tag{16}$$

in which x_{mean} is the mean value of velocity gradient in the domain and σ is the standard deviation of x. $c_{threshold}$ is an input parameter set to 0.25.

A base mesh size of 1 mm is used in the whole simulation domain. Additional mesh refinement is provided by applying four layers of 0.5 mm cells to the piston, liner and valve-seat walls. Velocity gradient is selected as the only adaptive refinement control parameter for SAM. With a combined use of SAM and boundary surface refinement, the peak cell count during the simulation of an engine cycle is 3 million. Figure 5 shows the status of meshing on the Y = 0 cut-plane that goes through the valve stems, at 100 degrees ATDC when the intake valve is completely open.

Flows during intake and compression strokes are of most interest, not only because of significant large-scale flow structures being present, but also due to their substantial impact on the flow conditions prior to spark ignition. During the intake stroke, cyclic variation in the intake jet structure causes subsequent variations in the flows within the combustion chamber. At 100 crank angle degrees after Top-Dead-Center (ATDC), the intake valve is completely open, and the whole intake jet structure can be characterized well. Also, the in-cylinder flow field at the end of the compression stroke affects the flame growth and propagation after spark ignition, thereby influencing combustion properties and engine performance. This flow field can be characterized at 300 degrees ATDC. In the simulations, velocity data at these two crank angles on the measurement planes are acquired using a monitor probe utility in the software, which collects data at points corresponding to the exact PIV measurement locations in the experiment.

The minimum number of simulated engine cycles required to obtain statistically converged LES results have been previously studied in the literature. Kuo *et al.* [6] indicated that 10 consecutive cycles (after neglecting the prior 10 cycles to stabilize from the impact of initial and boundary conditions) are sufficient for qualitative comparison between PIV and LES data. Ameen *et al.* [7] suggested that data from 20 consecutive cycles are sufficient to capture the cyclic variability during the gas exchange processes using their LES simulations. Considering these findings, 20 consecutive cycles of LES simulations are performed in the present work to form the statistical data base for analysis. Five prior cycles of data are neglected to exclude the impact from initialization, in view that the thermodynamic results after these excluded cycles become statistically stable. In order to examine the effects of LES SGS models and numerical schemes for momentum convection, four simulation sets are considered, and the test matrix is summarized in Table 2.

FIGURE 5 CFD mesh shown on the cut-plane at Y = 0 mm, at 100 degrees ATDC when intake valve is completely open. Mesh refinement due to use of SAM along the intake jet and fixed layers of refined cells near wall surfaces are visualized.

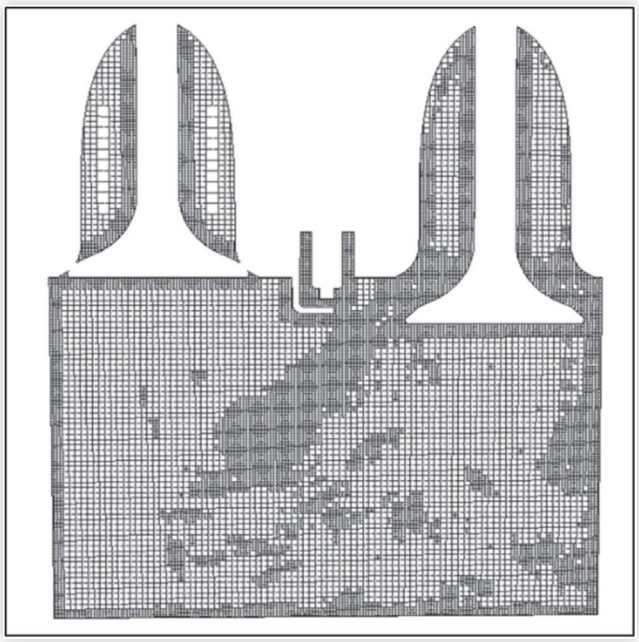

TABLE 2 Test Matrix used for LES simulation.

Simulation Set	1	2	3	4
LES model	LES-Smagorinsky	LES-Smagorinsky	Implicit LES	Implicit LES
Cs	0.17	0.17	0	0
Numerical Scheme	QSOU	CD	QSOU	CD

Results and Discussion

In each engine cycle, simulation starts at the onset of the intake stroke, when the piston is at TDC and the intake valve is opening. After completing the intake, compression, expansion and exhaust strokes, the cycle ends and the next cycle starts. The first engine cycle is initiated with the measured in-cylinder pressure and temperature data and with the assumption of quiescent chamber flows prior to the opening of the intake valve. The subsequent engine cycles are simulated in a consecutive manner and without interruption, such that no numerical assumptions are introduced when a new cycle starts. A total of 25 cycles are simulated, and the first 5 cycles are not included in the analysis to remove any influence from the initialization. The remaining 20 consecutive cycles are considered as a statistical representation of the whole set of (256) cycles measured in the experiment. The statistical convergence using 20 cycles' data in the simulation is verified in Appendix (A).

To validate the simulation setup, several global thermodynamic properties, such as the maximum in-cylinder pressure, temperature and trapped mass are examined. Figure 6 shows variations of these properties from the 20 consecutive engine cycles simulated. While there are cyclic variations observed in each set of simulations, the degrees of variations are very low in general. The very close amounts of trapped mass among different cycles indicate that the outcomes of gas exchange processes are predicted consistently. The consistent peak temperatures in the cylinder indicate that the settings of heat transfer boundary conditions and inflow/outflow conditions result in consistent amounts of thermal energy predicted at the TDC of each cycle.

FIGURE 6 Maximum in-cylinder pressure, trapped mass, and peak in-cylinder temperature predicts by four sets of simulations in 20 consecutive engine cycles.

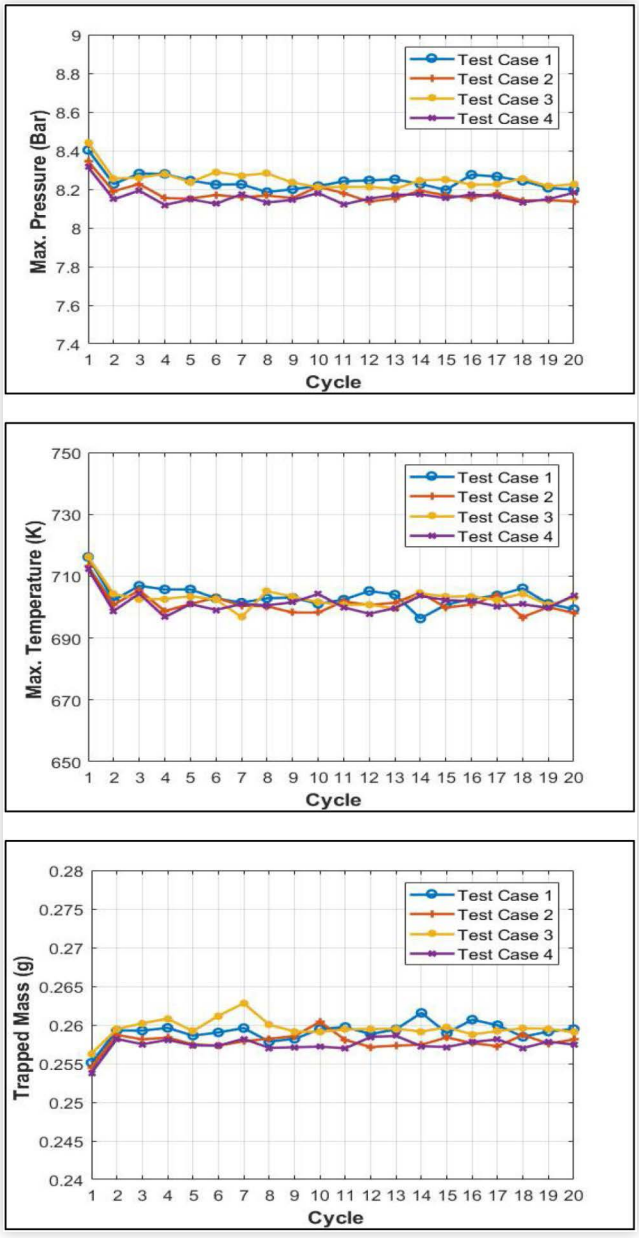

The predicted cycle-averaged peak pressures in the four sets of simulations show some differences due to the different SGS models and numerical schemes used; however, the deviations from the measured cycle-averaged values are within 2.4%. The coefficient of variance (defined as the ratio of standard deviation over the mean) of cyclic peak pressure is around 0.5-0.6%, which is on the same order of magnitude but somewhat higher than the measured one. The deviations of cycle-averaged trapped mass from the measurement are within 1.2%, as summarized in Table 3.

The deviations with experiment are thought to be due to the uncertainties in setting the compression ratio and heat transfer boundary conditions. The geometric compression ratio of the TCC-III engine is 10.0, while its "effective" compression ratio is 8.0 [22]. Temperatures at the solid wall boundaries are not available from the experiment specifications. In the simulations, the geometric compression ratio is set as 9.9, and constant wall temperatures are specified at the liner, cylinder head (and spark plug), and piston to calculate heat-transfer correlations in the boundary layer. A combination of these settings ensures that the best overall agreement between the predicted in-cylinder pressure, trapped mass and temperature traces and the measurements is reached. The settings could be improved with better knowledge of the wall temperature distribution as well as its variation in time, from either experiment or a conjugate-heat-transfer simulation.

TABLE 3 Cycle-averaged in-cylinder peak pressure, coefficient of variance of cyclic peak pressure, cycle-averaged peak temperature and trapped mass from the measurement and the four sets of LES simulations.

	Cycle-averaged Peak Pressure (bar)	Coefficient of Variance of Cyclic Peak Pressure (%)	Cycle-averaged Peak Temperature (K)	Cycle-averaged Trapped Mass (g)
Experiment	8.118	0.23	714.12	0.2582
Set 1	8.241	0.58	703.49	0.2591
Set 2	8.176	0.57	702.71	0.2579
Set 3	8.251	0.63	703.07	0.2596
Set 4	8.133	0.51	701.47	0.2575

To examine the in-cylinder pressure trace throughout one engine cycle, the predicted pressure traces from the 20 consecutive cycles are averaged, and compared to the experimental pressure averaged over 256 cycles. As shown in Figure 7, the predicted averaged pressure traces in all the test cases are in good agreement with the experimental average during the compression and expansion strokes.

FIGURE 7 In-cylinder averaged pressure trace in one engine cycle in simulation and experiment.

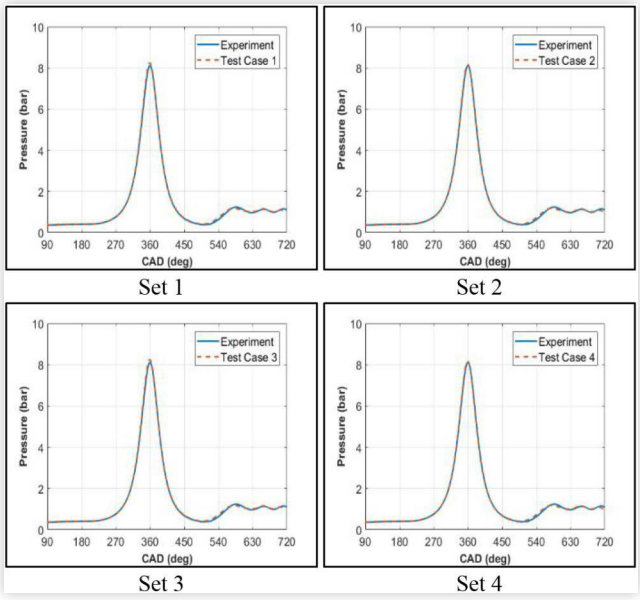

Averaged in-cylinder trapped mass and temperature from all LES simulations and experimental measurements are shown in Figures 8 and Figure 9, respectively. All the test cases correctly predict the averaged in-cylinder trapped mass. Simulations somewhat under-predict the amount of mass flowing into the cylinder due to negative pressure difference when the exhaust valve is opening, but the end mass after the whole exhaust stroke is predicted precisely. The overall trend of in-cylinder averaged temperature is captured by all the simulation setups. Deviation in the values of average temperature can be explained as an effect of using constant and uniform wall temperatures throughout the simulation.

In addition, the averaged peak pressure occurred at 1.5 crank angle degrees prior to TDC in the measurement [22], which is thought to be due to the heat transfer and blowby effects [29]. While the simulation models heat transfer, the blowby effects are not modeled due to omission of the ring pack and crevice regions.

Despite the uncertainties and simplifications in the simulation setup, the averaged thermodynamic results agree well with the experimental data in general, which validates the simulation settings for detailed flow field analysis. Quantitative comparisons of spatially resolved velocity vector field between LES and PIV measurements were then conducted by the following methods:

1. Statistical Method:

Statistical quantities of ensemble average and RMS of velocity are compared at two different crank angles, which are 100 and 300 degrees ATDC. The magnitude of mean and RMS velocity and the relevance index of the flow structures are examined.

2. Proper Orthogonal Decomposition Analysis:

Quantitative comparison between energy fractions and modes is done at the two crank angles. In this study, phase dependent 2D POD is carried out for LES results and PIV measurement data.

FIGURE 8 In-cylinder averaged trapped mass in one engine cycle in simulation and experiment.

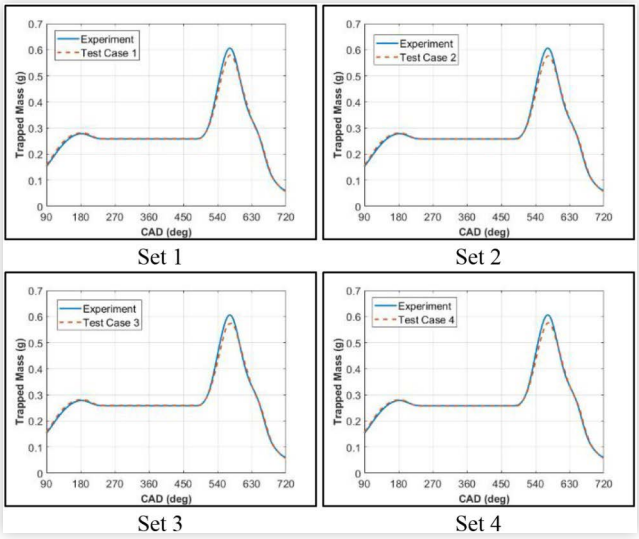

FIGURE 9 In-cylinder averaged temperature trace in one engine cycle in simulation and experiment.

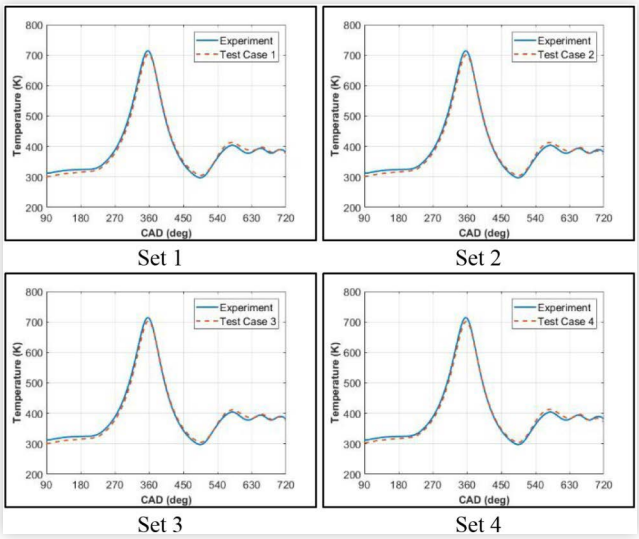

Results at Y = 0, 100 Degrees ATDC

Figure 10 compares the ensemble-averaged velocity field for all four test cases on the Y = 0 plane at 100 degrees ATDC, when the piston is moving downwards during the intake stroke and the intake valve is completely open. The measurement plane Y = 0 is positioned right at the center of the combustion chamber and cuts through both the intake and exhaust valves. As a result, an intake "jet" flow structure is revealed from the 2-D velocity field. Relevance index is calculated by correlating the prediction and measurement, using Eq. (8).

From the mean velocity flow field and the results of relevance indices, all the simulations qualitatively capture the intake jet structures. Presence of the mean velocity region at 80 m/s (colored by the red contour level) can be seen in the simulation results of all the settings as well as in the measurements, indicating that the mean velocity of the flow exiting the intake valve gap has been captured correctly by the simulations.

The relevance indices are in the range of 0.75 to 0.80, which shows room for improvement. The simulated jet penetrates into the cylinder in an almost uniform direction, unlike in the measurements where the end portion of the jet bends downward as it is entrained in a swirling structure. In the simulations, some swirling flow structures are observed but they are somewhat disconnected from the jet tip. As a result, the simulations under-predict the length of the jet.

Figure 11 shows the velocity vectors of mean flow field from the PIV data and Set 3 simulation results, as well as the relevance index between the two. Velocity vector arrows display flow structures, whereas lengths of the vector arrow represent the local velocity magnitude. Set 3 results, which

FIGURE 10 Mean velocity field at Y = 0 and 100 degrees ATDC during the intake stroke. The simulation results from four sets of model settings are compared with the PIV measurements. Relevance indices are summarized in the table.

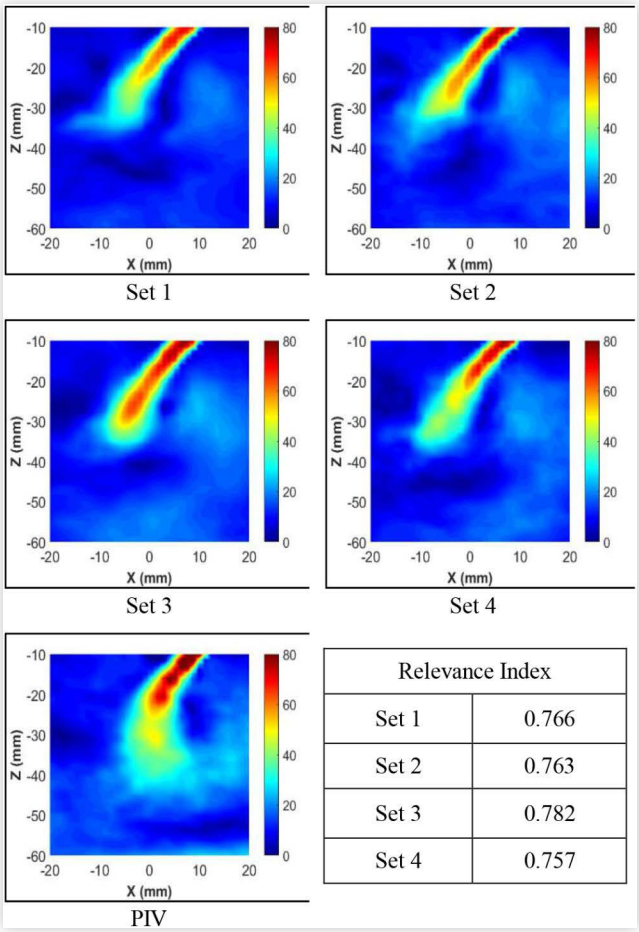

Relevance Index	
Set 1	0.766
Set 2	0.763
Set 3	0.782
Set 4	0.757

have the highest value of relevance index in all simulations, fairly capture major flow structures such as the intake jet and the vortex behind it. The predicted flow structures show similarity with the measurement, resulting in high relevance index in the jet region. However, the magnitude of the vortex is under-predicted, and both the predictions of vortex center location and vortex radius show some discrepancy from the measurement, which degrades the local relevance index. Deeper mesh refinement adaptive to the velocity field and within the valve gap is expected to resolve the intake jet structures better and improve the relevance index results. However, the increase of computational cost for each engine cycle would also be expected.

Shown in Figure 12, values of relevance indices for the RMS velocity field at 100 degrees ATDC indicate qualitatively good agreement in the fluctuating flow structures between the simulations and measurements. Strong turbulence intensity is observed in the diffusive regions surrounding the jet flow, which is consistently predicted by all the simulation settings. Note that the relevance index reflects the similarity of the local flow structure rather than the velocity magnitude. The magnitude of maximum RMS velocities predicted by Sets 2 and 4 agree well with the PIV data, while

FIGURE 11 Velocity vectors of mean velocity field at Y = 0 and 100 degrees ATDC during the intake stroke, from PIV measurements and Set 3 simulation results. The distribution of relevance indices in the flow field is also shown. The overall relevance index between the two fields (which is an arithmetic average of the local relevance indices from all the data points) is 0.782.

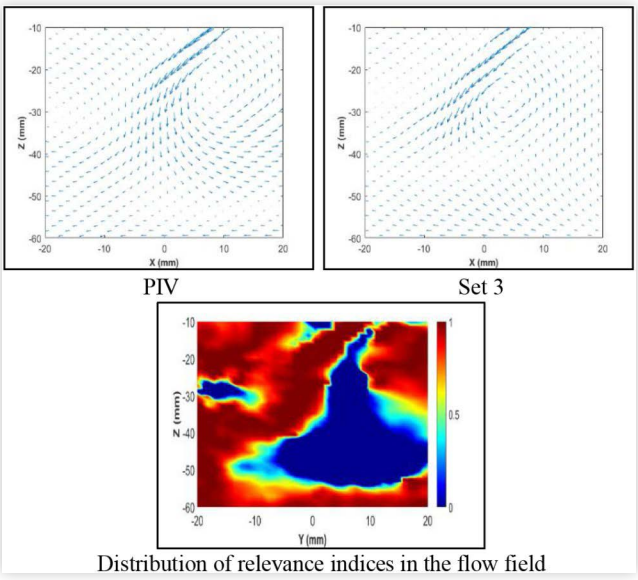

Sets 1 and 3 somewhat under-predict the peak RMS value. This is because the central differencing scheme has a higher order of accuracy than the QSOU scheme and lower numerical diffusion in solving the momentum transport processes [26], [12].

Figure 13 shows that the kinetic energy fractions of all POD modes from the simulations agree well with those from the PIV data. Energy fraction of the most energetic mode (mode #1) predicted by simulation is very close to the experimental measurement, indicating that the energy contained in the mean flow field is predicted correctly. Energy contained in higher modes is an order-of-magnitude smaller than that in the 1st mode, and this trend is correctly captured in the simulations. Simulation setting #4 predicts the most similar energy fraction profile compared to the experiment data.

To examine the flow patterns of each POD mode obtained from the measured PIV data and the simulations, Appendix (B) includes a short discussion.

Results at X = 0, 100 Degrees ATDC

Another examination of the flow field during intake is made at the X = 0 plane, which passes through the spark plug and is stationed between the intake and exhaust valves. At 100 degrees ATDC, characteristics of the 2-D flow field reveal the impact of momentum from the intake jet. Figures 14 and 15 show the ensemble-averaged and RMS of velocity field from the LES simulations and PIV measurements, respectively.

FIGURE 12 RMS velocity field at Y = 0 and 100 degrees ATDC during the intake stroke. The simulation results from four sets of model settings are compared with the PIV measurements. Relevance indices are summarized in the table.

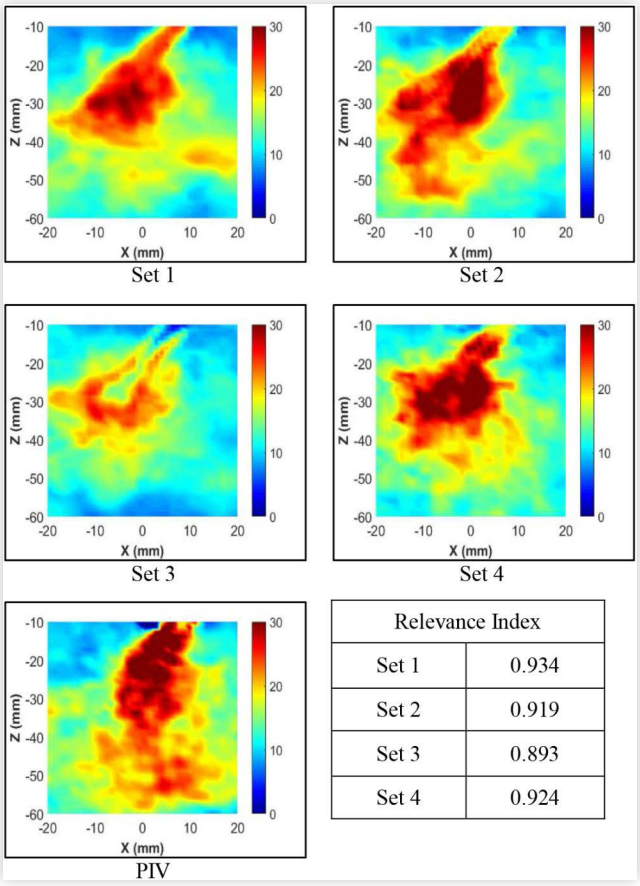

Relevance Index	
Set 1	0.934
Set 2	0.919
Set 3	0.893
Set 4	0.924

FIGURE 13 POD analysis of the 2-D flow field at Y = 0 and 100 degrees ATDC showing the energy fraction of each POD mode.

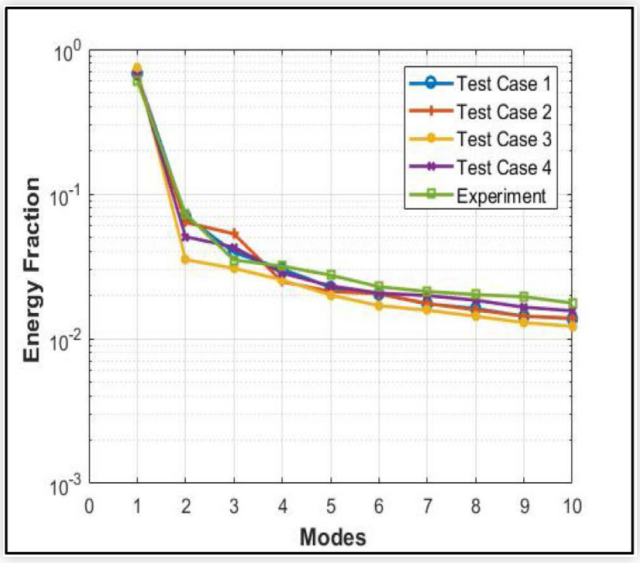

FIGURE 14 Mean velocity field at X = 0 and 100 degrees ATDC during the intake stroke. The simulation results from four sets of model settings are compared with the PIV measurements. Relevance indices are summarized in the table.

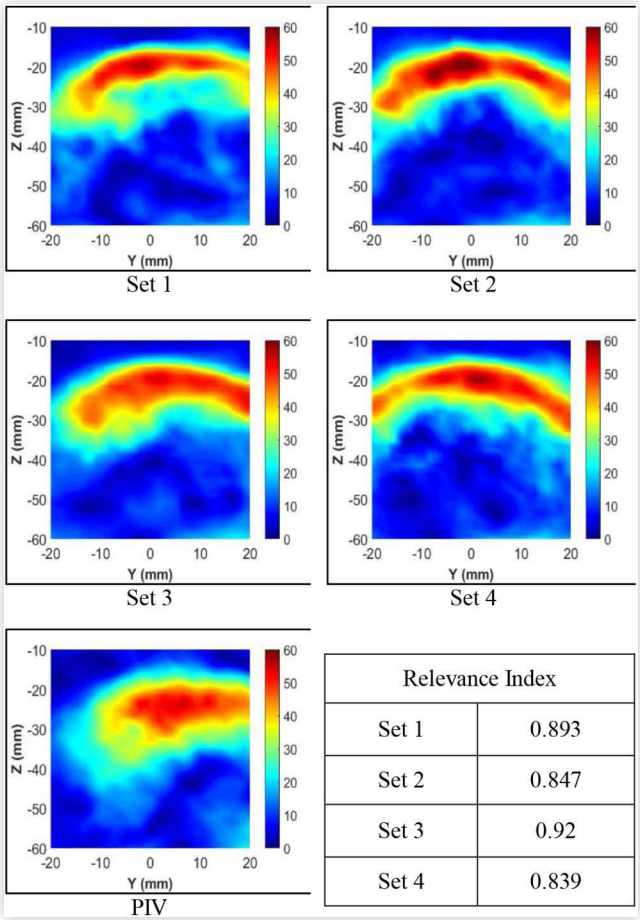

Relevance Index	
Set 1	0.893
Set 2	0.847
Set 3	0.92
Set 4	0.839

All test cases qualitatively capture the distributions of mean velocity as measured. This is evidenced by the good relevance indices in the mean velocity field. The momentum impact from the intake jet takes place in the region between Z = −5 mm and −30 mm, which is consistently observed in the simulations and measurements. From the measurement data, the momentum distribution is somewhat asymmetric about the Y = 0 plane, and this is captured better using the QSOU scheme than using the central differencing scheme. As a result, Sets 1 and 3 report higher relevance indices with respect to the PIV data. In addition, the distribution of velocity magnitude is better captured in Set 3. The momentum in Sets 2 and 4 are more symmetrically distributed relative to the Y = 0 plane, and the peak mean velocity is somewhat over-predicted. Recall that the downward bending of the intake jet as shown in the PIV data in Figure 10 is not very well predicted by all the simulation settings. As a result, the predicted momentum impact regions on the X = 0 plane (which correspond to the local jet thickness) are narrower.

In view of the RMS velocity field (Figure 15), very good relevance indices are reported, indicating that the fluctuating flow structures induced by the intake jet are consistent between simulations and measurements. The central difference scheme predicts higher magnitude of velocity fluctuation than the QSOU does, while the predicted magnitude using

FIGURE 15 RMS velocity field at X = 0 and 100 degrees ATDC during the intake stroke. The simulation results from four sets of model settings are compared with the PIV measurements. Relevance indices are summarized in the table.

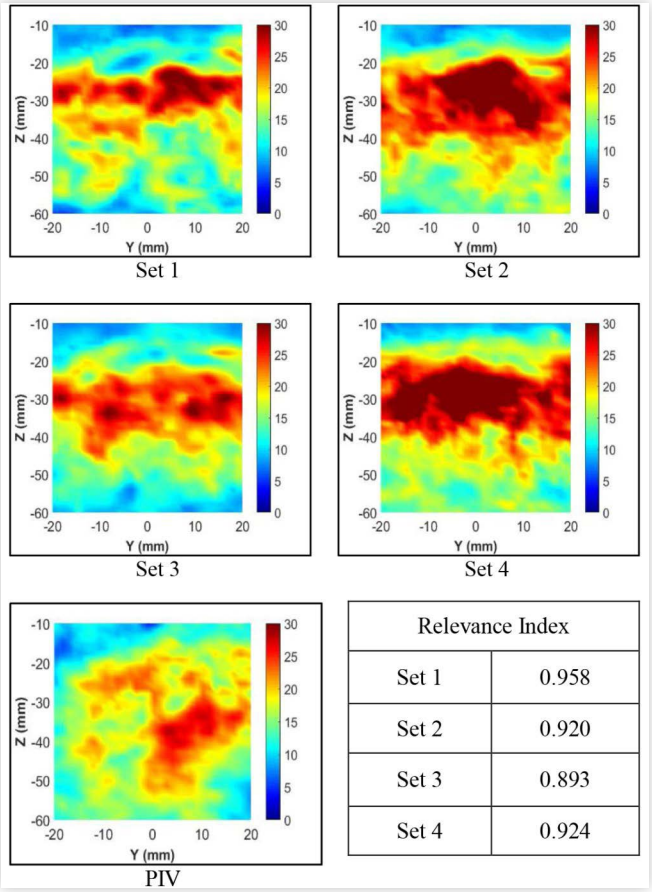

Relevance Index	
Set 1	0.958
Set 2	0.920
Set 3	0.893
Set 4	0.924

the QSOU scheme is closer to that measured. As is seen in the mean flow field, the simulation results are more symmetric about the Y = 0 plane compared to the measured data.

Figure 16 (Left) compares the predicted kinetic energy fractions of all the POD modes against the measurement. The trend of decaying energy distributed in higher modes is captured well by all the simulation settings. Simulations using the central differencing scheme predict higher energy in the 2nd mode, corresponding to the observation that they predict larger RMS velocity. Figure 16 (Right) shows the absolute value of relevance indices relating the predicted and measured flow field in each POD mode. Due to the resemblance between the 1st POD mode and the mean flow, the relevance indices of the 1st mode are close to those of the mean flow as discussed above. The relevance indices of higher modes are mostly within the range of 0.70~0.80, indicating reasonable predictions of the flow structures in these modes, too.

Overall, in predicting the intake flow characteristics, the impacts from the numerical schemes of momentum convection are more obvious than those from the SGS model settings. The central difference scheme predicts larger turbulent intensity in general, whereas the QSOU scheme captures the asymmetric intake jet impact region better. We do not see significant differences between Smagorinsky and the implicit

FIGURE 16 POD analysis of the 2-D flow field at X = 0 and 100 degrees ATDC. Left: energy fraction of each POD mode; Right: relevance index between the predicted and measured POD mode.

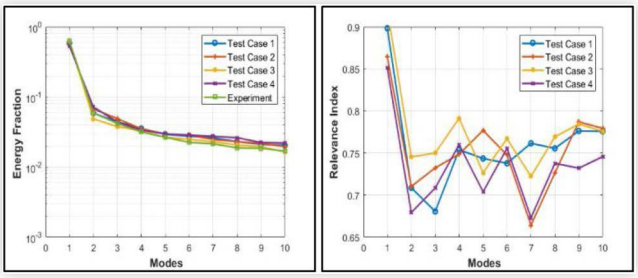

LES models, except that the latter predicts better mean flow structure and velocity magnitude on the X = 0 plane.

Results at Y = 0, 300 Degrees ATDC

Figures 17 and 18 present the ensemble-averaged and RMS velocity field on the Y = 0 plane at 300 degrees ATDC,

FIGURE 17 Mean velocity field at Y = 0 and 300 degrees ATDC during the compression stroke. The simulation results from four sets of model settings are compared with the PIV measurements. Relevance indices are summarized in the table.

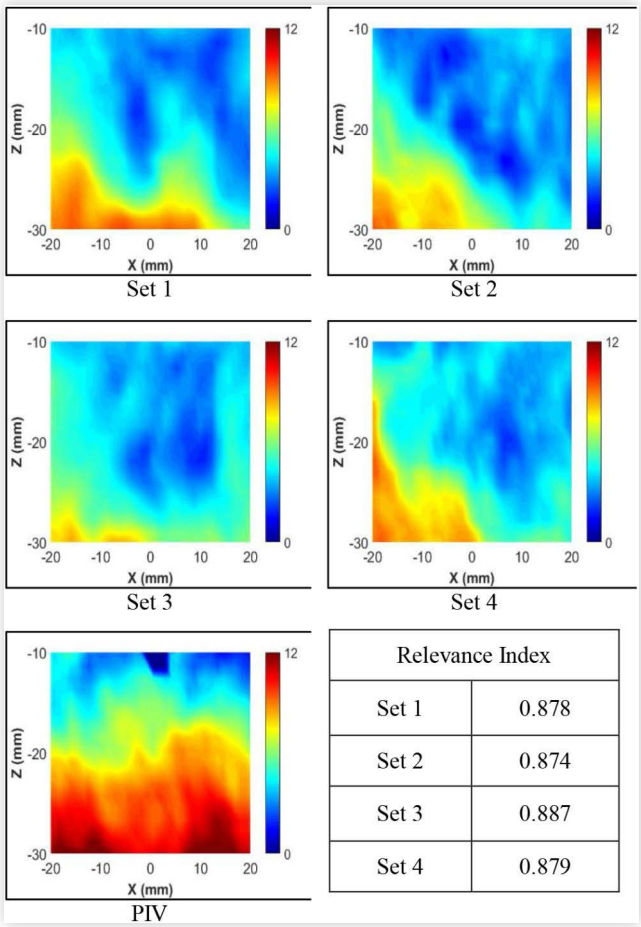

Relevance Index	
Set 1	0.878
Set 2	0.874
Set 3	0.887
Set 4	0.879

FIGURE 18 RMS velocity field at Y = 0 and 300 degrees ATDC during the compression stroke. The simulation results from four sets of model settings are compared with the PIV measurements. Relevance indices are summarized in the table.

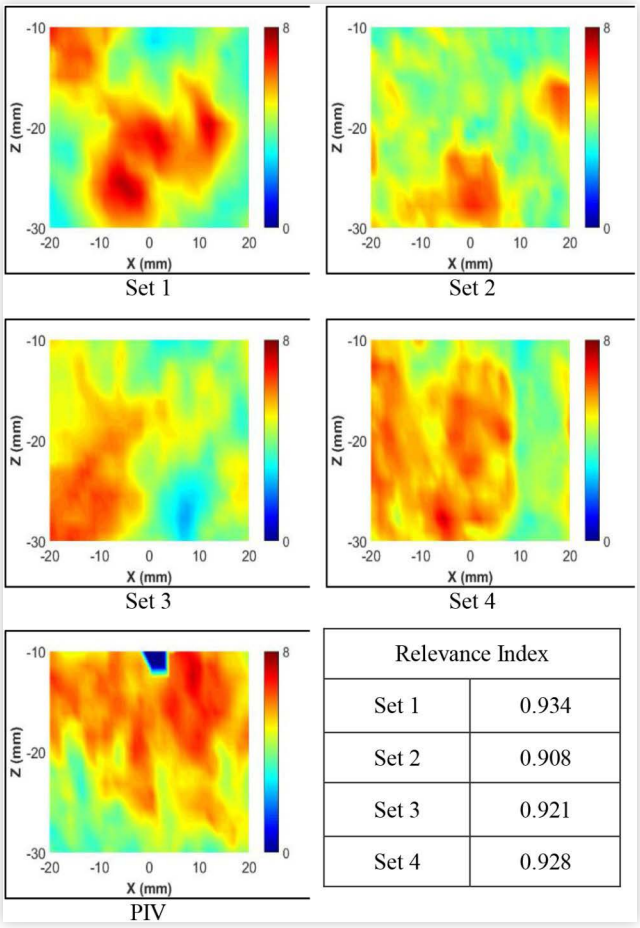

Relevance Index	
Set 1	0.934
Set 2	0.908
Set 3	0.921
Set 4	0.928

FIGURE 19 Velocity vectors of mean velocity field at Y = 0 and 300 degrees ATDC during the compression stroke, from PIV measurements and Set 3 simulation results. The distribution of relevance indices in the flow field is also shown. The overall relevance index between the two fields is 0.887.

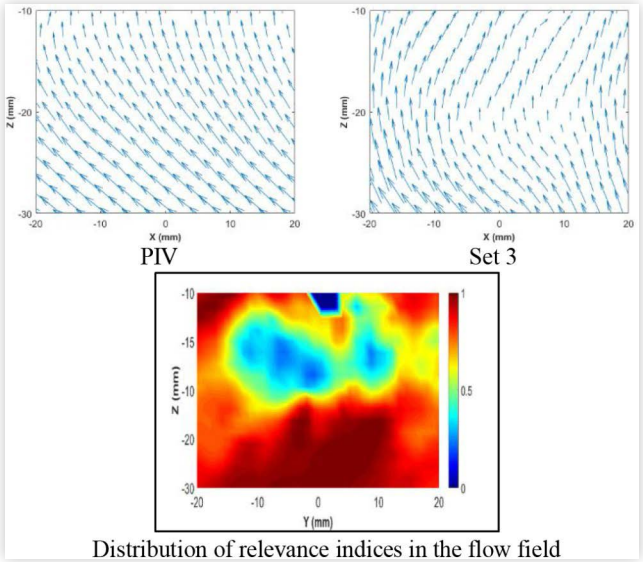

which represents the compression stroke when both intake and exhaust valves are completely closed. In both mean and RMS results, high relevance indices correlating the predictions and the measurements are achieved, indicating that the predicted flow structures in the combustion chamber induced by piston compression are similar to the experimental data.

In both simulation and measurement results, the highest mean velocity magnitude is observed at the bottom of the measurement plane, which is close to the piston. The measured maximum mean velocity is on the order of 12 m/s and is much larger than the instantaneous piston moving speed (~4 m/s), indicating the presence of strong tumble and turbulent motions. The maximum mean velocity is somewhat under-predicted in the simulations. Measurement also shows a fairly uniform distribution of mean velocity magnitude along the x direction (parallel to the piston surface). However, in simulations, the distributions of mean velocity magnitude are non-uniform. Similar results have been reported in the work of Ameen *et al.* [10] when a mesh size of 0.25 mm was employed near the piston walls. It is expected that an increase in the near-wall mesh resolution would be helpful for more precise prediction of mean velocity magnitude.

Simulation results in the RMS velocity field achieve high relevance indices with respect to the measurements. Magnitudes of the peak RMS velocities predicted by all the test cases are close to the values measured by PIV. In the measurement, larger RMS velocity is observed in the upper portion of the measurement plane where the mean flow speed is lower. This trend is not clearly observed in the simulation results, in which larger RMS velocity is more likely to appear in places where mean flow speed is also large. Finer mesh resolution and more engine cycles simulated might increase the accuracy of the RMS velocity flow field prediction.

Further examination of the mean flow structures is made in Figure 19, where the velocity vectors of the mean flow field are visualized, and the relevance index between the measured and simulated flow field is calculated. The measurement shows a fairly uniform motion towards the -X direction, indicating presence of a clockwise tumble motion above the piston. The tumble is qualitatively captured by the simulation, resulting in a high overall relevance index (0.887) between the two fields.

Figure 20 (Left) presents the predicted kinetic energy fractions of all the POD modes compared against the measurement. Simulations capture the correct trend in energy distribution among different modes. The predicted 1st modes contain lower energy that that in the measurement, corresponding to the larger mean flow magnitude observed in the PIV data as shown in Figure 17. As a result, the predicted results contain larger energy in higher modes. Figure 20 (Right) shows the absolute values of relevance indices computed by correlating the predicted and measured flow velocities for each POD mode. In general, relevance indices fall within the range of 0.70~0.80, indicating fairly good resemblance between the predicted and measured flow structures.

FIGURE 20 POD analysis of the 2-D flow field at Y = 0 and 300 degrees ATDC. Left: energy fraction of each POD mode; Right: relevance index between the predicted and measured POD mode.

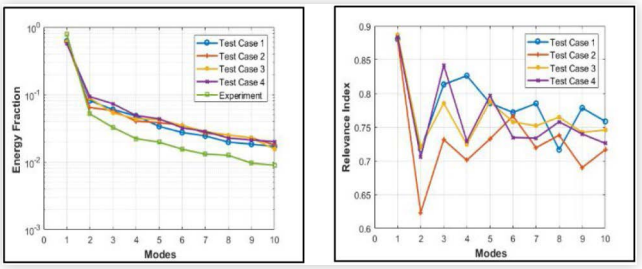

Summary and Conclusion

To summarize, this study evaluates the use of Large-eddy simulations of turbulent flows in a motored SI engine to predict cycle-to-cycle variation. LES results are compared with experimental measurements using a comprehensive set of statistical criteria. The simulations are set up to mimic the engine used in the experiment in terms of the engine geometry, inflow and outflow boundary conditions, and engine operating conditions. The simulation setup is validated by the averaged pressure trace as well as averaged peak pressure, temperature and trapped mass in the combustion chamber. A total of 20 consecutive engine cycles are simulated to represent a statistical ensemble of many more cycles in the measurements. An engineering-level mesh resolution (0.5 mm minimum) is chosen for all the simulations in this study.

Detailed flow velocity data are collected at two planes (Y = 0 and X = 0, respectively) at the center of the combustion chamber, where various statistical metrics are employed to examine the predicted mean and variance of the flows in comparison to the measurements. The metrics include mean and RMS of the 2-D velocity magnitude, relevance index relating flow structures between simulation and measurement, and characteristics of POD modes extracted from the flow field. The comparisons are made at two crank angle degrees, highlighting intake flows and the flows during piston compression, respectively. The main findings are:

1. *Intake flows*: simulations capture the intake flows exiting the valve gaps in terms of the mean velocity magnitude and the RMS flow structures. Energy fractions of the POD modes agree well with experimental data. The central difference scheme for momentum convection predicts larger turbulent intensity and RMS velocity magnitude, whereas the QSOU scheme offers better prediction of the asymmetric momentum impact projected on the X = 0 plane. The prediction by implicit LES method is slightly better than the Smagorinsky model, but the differences are small. Improvement is needed regardless of model settings in predicting the tip structure of the intake "jet" as seen in the mean flow field.
2. *Flows during piston compression*: simulations capture the flow structures in mean and RMS velocity field as revealed by the high relevance indices between computational and experimental results. Influences from the numerical schemes as well as SGS models are not obvious. The magnitude of mean flow velocity is somewhat under-predicted, resulting in lower kinetic energy contained in the 1st POD mode.

In both flow situations, increasing the dynamic mesh refinement depth and overall mesh resolution is expected to lead to better predictions, which will be the focus of our future work. On the other hand, the results obtained using the current mesh resolution indicate that good agreement with the measurements is achieved in many aspects, such as the energy fractions in each POD mode and the relevance indices in the RMS velocity field. Using the current simulation settings, the implicit LES model and the QSOU scheme for momentum convection is preferred, due to its better prediction of the mean flow field during intake. Other areas for future studies include validation of the flow field results under different engine speed, and validations using data from a fired engine.

References

[1] Heywood, J. B., "*Internal Combustion Engine Fundamentals, International Edition*," (Singapore, McGraw-Hill, 1988), 829-839, ISBN-10: 0-07-100499-8.

[2] Ozdor, N., Dulger, M., and Sher, E., "Cyclic Variability in Spark Ignition Engines a Literature Survey," SAE Technical Paper 940987, 1994, doi:10.4271/940987.

[3] Haworth, D.C., "Large-Eddy Simulation of in-Cylinder Flows," *Oil & Gas Science and Technology - Rev. IFP* 54(2):175-185, 1999, doi:10.2516/ogst:1999012.

[4] Rutland, C.J., "Large-Eddy Simulations for Internal Combustion Engines - a Review," *International Journal of Engine Research* 12(5):421-451, 2011, doi:10.1177/1468087411407248.

[5] Yang, X., Gupta, S., Kuo, T.-W., and Gopalakrishnan, V., "RANS and Large Eddy Simulation of Internal Combustion Engine Flows - a Comparative Study," *Journal of Engineering for Gas Turbines and Powers* 136(5):-051507, 2013, doi:10.1115/1.4026165.

[6] Kuo, T.-W., Yang, X., Gopalakrishnan, V., and Chen, Z., "Large Eddy Simulation (LES) for IC Engine Flows," *Oil & Gas Science and Technology - Rev. IFP Energies nouvelles* 69(1):61-81, 2013, doi:10.2516/ogst/2013127.

[7] Ameen, M. M., Yang, X., Kuo, T.-W., Xue, Q., Som, S., "LES for Simulating the Gas Exchange Process in a Spark Ignition Engine," *ASME 2015 Internal Combustion Engine Division Fall Technical Conference, Paper No. ICEF2015-1002*, pp. V002T06A001, 2015, doi:10.1115/ICEF2015-1002.

[8] Ameen, M.M., Yang, X., Kuo, T.-W., and Som, S., "Parallel Methodology to Capture Cyclic Variability in Motored Engines," *International Journal of Engine Research* 18(4): 366-377, 2017, doi:10.1177/1468087416662544.

[9] Van Dam, N., Sjöberg, M., Zeng, W., and Som, S., "Parallel Multi-Cycle LES of an Optical Pent-roof DISI Engine under

Motored Operating Conditions," *presented at the 2017 ASME Internal Combustion Engine Fall Technical Conference, USA, October 15-18*, 2017.

[10] Ameen, M. M., Mirzaeian, M., Millo, F., and Som, S., "Numerical Prediction of CCV in a PFI Engine using a Parallel LES Approach," *presented at the 2017 ASME Internal Combustion Engine Fall Technical Conference, USA, October 15-18*, 2017.

[11] Kodavasal, J., Moiz, A. M., Ameen, M. M., and Som, S., "Machine Learning Analysis of Factors Impacting Cycle-to-Cycle Variation in a Gasoline Spark-Ignited Engine," *presented at the 2017 ASME Internal Combustion Engine Fall Technical Conference, USA, October 15-18*, 2017.

[12] Tsang, C., Wang, Y., Wang, C., Shelburn, A. et al., "Evaluation and Validation of Large-Eddy-Simulation (LES) for Gas Jet and Sprays," SAE Technical Paper 2017-01-0844, 2017, doi:10.4271/2017-01-0844.

[13] Zhao, L., Moiz, A. A., Som, S., Fogla, N. et al. "Examining the Role of Flame Topologies and In-Cylinder Flow Fields on Cyclic Variability in Spark-Ignited Engines Using Large-Eddy Simulation," *International Journal of Engine Research* (in press), 2017, doi:10.1177/1468087417732447.

[14] Schiffmann, P., Gupta, S., Reuss, D., Sick, V. et al., "TCC-III Engine Benchmark for Large-Eddy Simulation of IC Engine Flows," *Oil & Gas Science and Technology - Rev. IFP Energies nouvelles* 71(3), 2016, doi:10.2516/ogst:2015028.

[15] Reuss, D.L., "Cyclic Variability of Large-Scale Turbulent Structures in Directed and Undirected IC Engine Flows," SAE Technical Paper 2000-01-0246, 2000, doi:10.4271/2000-01-0246.

[16] Van Dam, N. and Rutland, C. J., "Understanding In-Cylinder Flow Variability Using Large-Eddy Simulations," *ASME 2015 Internal Combustion Engine Division Fall Technical Conference, Paper No. ICEF2015-1103*, pp. V002T06A014, 2015, doi:10.1115/ICEF2015-1103.

[17] Chen, H., Reuss, D.L., and Sick, V., "On the Use and Interpretation of Proper Orthogonal Decomposition of In-Cylinder Engine Flows," *Measurement Science and Technology* 23(8):085302, 2012, doi:10.1088/0957-0233/23/8/085302.

[18] Liu, K. and Haworth, D., "Development and Assessment of POD for Analysis of Turbulent Flow in Piston Engines," SAE Technical Paper 2011-01-0830, 2011, doi:10.4271/2011-01-0830.

[19] Chen, H., Reuss, D.L., Hung, D., and Sick, V., "A Practical Guide for Using Proper Orthogonal Decomposition in Engine Research," *International Journal of Engine Research* 14(4):307-319, 2013, doi:10.1177/1468087412455748.

[20] Buhl, S., Hartmann, F., and Hasse, C., "Identification of Large-Scale Structure Fluctuations in IC Engines Using POD-based Conditional Averaging," *Oil & Gas Science and Technology - Rev. IFP Energies nouvelles* 71(1), 2016, doi:10.2516/ogst/2015021.

[21] Sick, V., et al., "A Common Engine Platform for Engine LES Development and Validation," *presented at LES4ICE: International Conference on LES for Internal Combustion Engine Flows, France, November 18-19*, 2010.

[22] Sick, V.Reuss, D. ,Yang, X. ,Kuo, T.-W. , and, "TCC-III CFD Input Data," https://deepblue.lib.umich.edu/handle/2027.42/108382, accessed Jul. 2017.

[23] Abraham, P., Reuss, D., and Sick, V., "High-Speed Particle Image Velocimetry Study of In-Cylinder Flows with Improved Dynamic Range," SAE Technical Paper 2013-01-0542, 2013, doi:10.4271/2013-01-0542.

[24] ANSYS Inc., "*ANSYS Forte (Version 18.2), Computer Software*," (San Diego, CA, ANSYS Inc., 2017).

[25] Amsden, A.A., O'Rourke, P.J., and Butler, T.D., "*KIVA-II: A Computer Program for Chemically Reactive Flows with Sprays*," (LA-11560-MS, Los Alamos National Laboratory, 1989).

[26] Tsang, C. and Rutland, C., "Effects of Numerical Schemes on Large Eddy Simulation of Turbulent Planar Gas Jet and Diesel Spray," *SAE International Journal of Fuels and Lubricants* 9(1):149-164, 2016, doi:10.4271/2016-01-0866.

[27] Sirovich, L., "Turbulence and the Dynamics of Coherent Structures. I. Coherent Structures," *Quarterly of Applied Mathematics* 45(3):561-571, 1987.

[28] Liang, L., Wang, Y., Shelburn, A., Wang, C. et al. "Applying Solution-Adaptive Mesh Refinement in Engine Simulations," *presented at the International Multidimensional Engine Modeling User's Group Meeting, April 11, USA*, 2016.

[29] Sick, V., University of Michigan, Personal Communication, Jun. 2017.

Contact Information

Devyani Patil
ANSYS Inc.
5930 Cornerstone Court West, Suite 230
San Diego, CA 92121, USA
(currently affiliated with John Deere)
Work phone: +1 906 275 8819
devyanip@mtu.edu
cpatildevyani21@gmail.com

Yue Wang, Ph.D.
ANSYS Inc.
5930 Cornerstone Court West, Suite 230
San Diego, CA 92121, USA
Work phone: +1 858 210 3202
yue.wang@ansys.com
yuewang05@gmail.com

Acknowledgments

The authors acknowledge that we have used the published engine setup and PIV experimental data of the TCC-III engine. The TCC engine work has been funded by General Motors University of Michigan Automotive Cooperative Research Laboratory, Engine Systems Division. The authors appreciate the comments of Prof. Volker Sick from University of Michigan in regard to the engine setup.

Definitions/Abbreviations

ATDC - After Top Dead Center

CAD - Crank Angle Degree

CCV - Cycle-to-Cycle Variation
CD - Central Difference
CFD - Computational Fluid Dynamics
COV - Coefficient Of Variance
LES - Large Eddy simulation
PIV - Particle Image Velocimetry
POD - Proper Orthogonal Decomposition
QSOU - Quasi Second Order Upwind
RMS - Root Mean Square
SAM - Solution Adaptive Meshing
SGS - Sub Grid Scale
SI - Spark Ignition
TCC - Transparent Combustion Chamber

Appendix (A)

When analyzing the simulation results, data from 20 concecutive engine cycles are used to compute the ensemble-averaged and RMS velocity field and POD modes. To make sure that the 20 cycles' data have reached statistical convergence in the averaged quantities, the averaged data from 10, 15, 18 cycles are examined, and summarized in Figures 21 and 22. Both the results averaged from 15 and 18 cycles are very close to those averaged from 20 cycles, as evidenced by very high relevance indices (0.998 and above). Therefore, it is decided that statistic convergence has been reached when 20 cycles of data are used.

FIGURE 21 Mean velocity field at Y = 0 and 100 degrees ATDC during the intake stroke. The simulation results averaged from 10, 15, 18 and 20 cycles are compared. Model setting #3 (see Table 2) is used. The relevance indices between the averaged velocity field using 10, 15, 18 cycles and that of 20 cycles are 0.995, 0.998, 0.999, respectively.

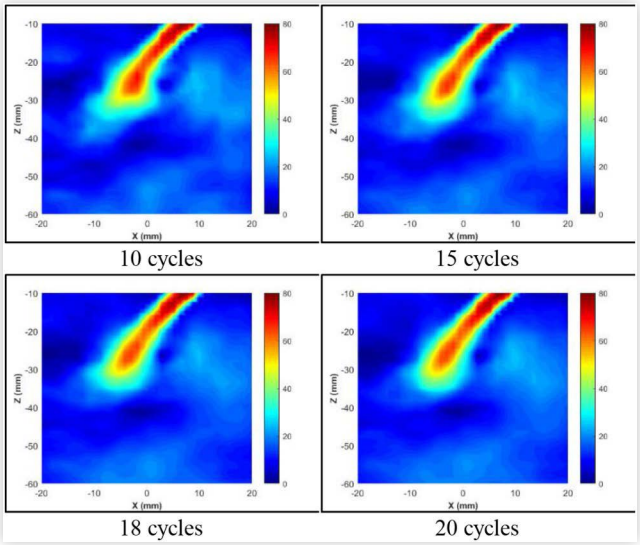

FIGURE 22 RMS velocity field at Y = 0 and 100 degrees ATDC during the intake stroke. The simulation results averaged from 10, 15, 18 and 20 cycles are compared. Model setting #3 (see Table 2) is used. The relevance indices between the averaged velocity field using 10, 15, 18 cycles and that of 20 cycles are 0.993, 0.998, 0.999, respectively.

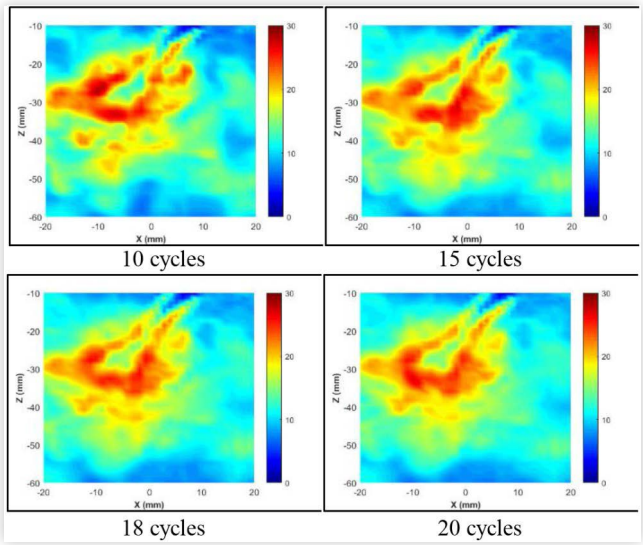

Appendix (B)

To further examine the simulation results using POD analysis, it is of interest to look into the flow patterns in each POD mode, and compare the prediction against the measurement. Figure 23 compares the first five POD modes extracted from the flow field at Y = 0 plane and 100 degrees ATDC. The POD modes, which correspond to f^m in Eq. (9) and (10), are unit vector field. The flow patterns contained in the 1st POD mode are analogous to those in the ensemble-averaged flow field. As discussed earlier, the intake jet structure is captured by the simulation, but the predictions of vortex radius and vortex center location on valve side need improvement. The predicted flow patterns in higher modes are qualitatively similar to the measured modes, although detailed flow structures vary locally.

FIGURE 23 POD modes extracted from the PIV-measured and simulated velocity field at Y = 0 and 100 degrees ATDC during the intake stroke. Only the first five modes are presented. Simulation results are obtained by model setting #3 (see Table 2).

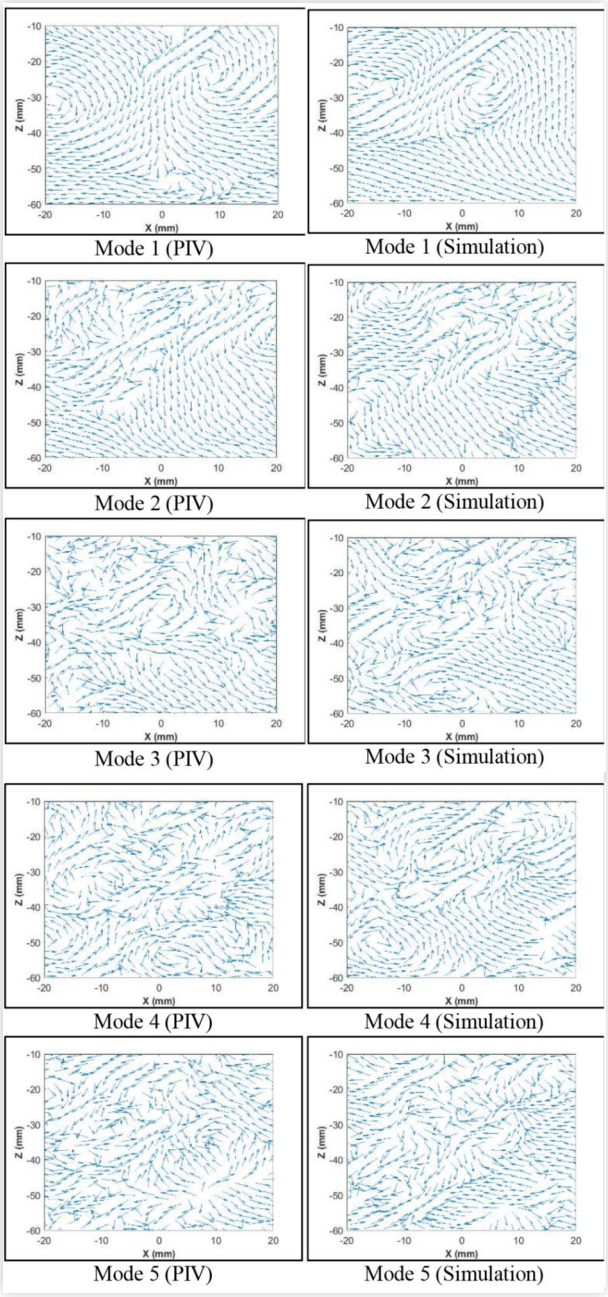

ISSN 0148-7191